

Orbital migration and circularization of tidal debris by Alfvén-wave drag: circumstellar debris and pollution around white dwarfs

YUN ZHANG (张韵) ¹, SHANG-FEI LIU (刘尚飞) ² AND DOUGLAS N.C. LIN (林潮) ^{3,4}

¹*Université Côte d’Azur, Observatoire de la Côte d’Azur, CNRS, Laboratoire Lagrange, Nice 06304, France*

²*School of Physics and Astronomy, Sun Yat-sen University, 2 Daxue Road, Tangjia, Zhuhai 519082, Guangdong Province, China*

³*Department of Astronomy and Astrophysics, University of California, Santa Cruz, USA*

⁴*Institute for Advanced Studies, Tsinghua University, Beijing, 100086, China*

(Received March 22, 2021; Revised April 24, 2021; Accepted May 11, 2021)

Submitted to ApJ

ABSTRACT

A significant fraction of white dwarfs (WDs) exhibit signs of ongoing accretion of refractory elements at rates $\sim 10^3\text{--}10^7$ kg s⁻¹, among which, 37 WDs were detected to harbor dusty debris disks. Such a concurrence requires not only fertile reservoirs of planetary material, but also a high duty cycle of metal delivery. It has been commonly suggested that this material could be supplied by Solar System analogs of Main Belt asteroids or Kuiper Belt objects. Here we consider the primary progenitors of WD pollutants as a population of residual high-eccentricity planetesimals, de-volatilized during the stellar giant phases. Equivalent to the Solar System’s long-period comets, they are scattered to the proximity of WDs by perturbations from remaining planets, Galactic tides, passing molecular clouds, and nearby stars. These objects undergo downsizing when they venture within the tidal disruption limit. We show quantitatively how the breakup condition and fragment sizes are determined by material strength and gravity. Thereafter, the fragments’ semi-major axes need to decay by at least ~ 6 orders of magnitude before their constituents are eventually accreted onto the surface of WDs. We investigate the orbital evolution of these fragments around WDs and show that WDs’ magnetic fields induce an Alfvén-wave drag during their periastron passages and rapidly circularize their orbits. This process could be responsible for the observed accretion rates of heavy-elements and the generation of circum-WD debris disks. A speculative implication is that giant planets may be common around WDs’ progenitors and they may still be bound to some WDs today.

Keywords: White dwarf stars (1799) — Minor planets (1065) — Exoplanet evolution (491) — Exoplanet dynamics (490)— Debris disks (363)

1. INTRODUCTION

After losing their red giant progenitors’ envelope, a significant fraction of white dwarfs (WDs) were detected to harbor residual planetary bodies, as revealed by the evidence of metal pollution in their spectra (Zuckerman et al. 2003; Koester et al. 2014), infrared excesses and metal emission lines from close-in debris disks (Zuckerman & Becklin 1987; Barber et al. 2012; Manser et al. 2020), and photometric and spectroscopic signatures of

transiting planetary material in close proximity to the WDs (Vanderburg et al. 2015; Xu et al. 2017; Manser et al. 2019; Vanderbosch et al. 2020). These phenomena can be readily explained by the tidal disruption and accretion of remnant planetary bodies (such as asteroids and comets) that were perturbed into nearly parabolic orbits with pericenters in proximity to their host WDs (Debes & Sigurdsson 2002; Jura 2003; Kratter & Perets 2012; Veras et al. 2015b; Chen et al. 2019; Malamud & Perets 2020). However, detailed dynamical processes connecting these planetary remnants around WDs with the planetary systems in the late stages of stellar evo-

lution remain poorly understood (e.g., Veras 2016, and references therein).

Due to the mass loss and size expansion of a host star in its post-main-sequence evolution, the orbiting objects migrate outward (Hadjidemetriou 1963; Adams et al. 2013) and some may be engulfed by the enlarging star on the giant branch (Schröder & Connon Smith 2008). These stars’ intensified luminosity also heats the surface of residual objects, sublimates and disperse their volatile contents. With the consideration of the time-varying giant-branch luminosities and the consequently intensified Yarkovsky effect, Veras et al. (2019) found the engulfment survivors generally have asymptotic orbital semi-major axes larger than 10–100 au. In order to form the observed circumstellar debris disks in the proximity of the WDs (with orbital semi-major axes on the order of one solar radius and small orbital eccentricities), substantial orbital migration and circularization of these objects and their tidal fragments are required.

A commonly held view is that remnant planetary bodies are grounded to μm -sized dust by WDs’ tidal effect (Jura 2003) and by collisional cascades (Kenyon & Bromley 2017) when they approach the WDs’ tidal radii. Subsequently, the μm -sized and smaller dust can be circularized near the tidal radius and be accreted onto the WDs by their radiation (Rafikov 2011; Veras et al. 2015b) and/or magnetic drag (Hogg et al. 2021) on relatively short timescales.

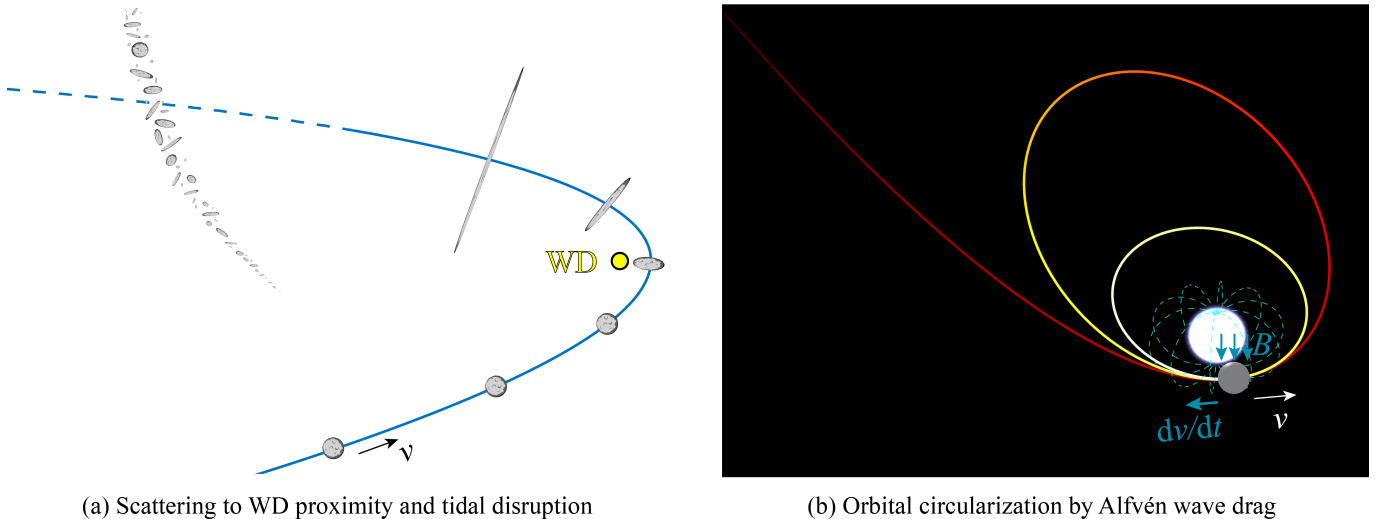
However, there is hardly any empirical constraint on the particle size distributions in the circumstellar debris of WDs (Farihi 2016) and it is likely that cm-sized grains to even km-sized objects could be common (Rafikov & Garmilla 2012; Vanderburg et al. 2015; Xu et al. 2017; Manser et al. 2019). In effect, the size distribution of tidal disruption debris highly depends on the granular constituents and material strength of the progenitor body. Wide-ranging observations and *in-situ* explorations have confirmed that most of Solar System small bodies, with diameters $\gtrsim 200$ m and $\lesssim 50$ km (which belong to one of the most common small body population in the Solar System), have rubble-pile structures, in which boulders and grains are held together mainly by gravitational forces (Richardson et al. 2002; Hestroffer et al. 2019). As revealed by recent space missions, the size of boulders and grains of rubble-pile bodies typically ranges from sub-cm to 100 m (e.g., Walsh et al. 2019) with individual material tensile strength on the order of 0.1–10 MPa (Pohl & Britt 2020). This level of material strength can help some large boulders to remain intact within the strength-free Roche radius (Holsapple & Michel 2008; Zhang & Lin 2020). Therefore, the tidal

debris of a rubble-pile body at WDs may have size distributions close to the size distribution of its constituents.

For a 100-km-sized body with an internal viscosity similar to that of molten rocks, tidal friction can circularize its orbit within appropriate timescales (O’Connor & Lai 2020). However, the stiff interior of the cm-sized grains to 100-m-sized boulders can not provide the required internal viscosity for tidal friction migration. WD radiation (Rafikov 2011; Veras et al. 2015b) and associated material sublimation (Veras et al. 2015a) are inefficient to circularize the orbits of decimeter-sized or larger particles. Therefore, other mechanisms are needed to account for the high-eccentricity migration of objects within this size range.

Around 8–20% of WDs currently have magnetic fields with strengths ranging from 10^3 to 10^9 G (Ferrario & Wickramasinghe 2005; Ferrario et al. 2015). The origin of WDs’ magnetic fields remains an outstanding issue (Isern et al. 2017). Observations (e.g., Hollands et al. 2015; Kawka et al. 2019) suggest a higher incidence of magnetism in WDs at low effective temperatures, which may indicate that magnetic fields has been amplified during the evolution of WDs. The presence of magnetic fields has a significant influence on the dynamics of μm -sized dust around WDs (Farihi et al. 2017; Hogg et al. 2021) and the consequent Ohmic heating and Lorentz drift can cause the decay of close-in orbits of asteroid-sized objects (Bromley & Kenyon 2019; Veras & Woloszczan 2019). In addition, the Alfvén wave emitted from an object orbiting a magnetic WD might also cause significant drag effects on its orbit (Drell et al. 1965), which will be examined in this study.

Here we investigate the role of material strength on the tidal fragmentation size distribution and examine the orbital migration of tidal debris by the Alfvén-wave drag in the proximity of WDs. The illustrative Figure 1 presents the two main processes considered in this study that attribute to the formation of circumstellar debris and pollution of WDs. We briefly recapitulate the dynamical evolution of fragments’ parent bodies under this scenario in Section 2. We establish, in Section 3, the tidal disruption condition around WDs and derive the survivor size for various material strength and pericenter distances. In Section 4, we analyze the orbital energy dissipation and migration of survivors within the possible size range under the effect of Alfvén-wave drag. In Section 5, dedicated numerical simulations are carried out to validate our analytic approximation. Taking these consideration together, we elaborate, in Section 6, the scenario of the transformation of long-period comets (LPCs) into circular debris close to the WDs. We summarize our results and discuss their implications regard-



(a) Scattering to WD proximity and tidal disruption

(b) Orbital circularization by Alfvén wave drag

Figure 1. A schematic of the dynamical evolution of remnant planetary bodies around a magnetic WD.

ing circumstellar debris and pollution at WDs in Section 7.

2. HIGH-ECCENTRICITY MIGRATION OF HEAVY-ELEMENTS' PARENT BODIES

In this paper, we adopt the scenario, as shown in Fig. 1, that debris disks and accreted refractory elements at WDs originated from remnant planetary bodies residing in regions analogous to the Kuiper belt and Oort cloud in the Solar System (Veras et al. 2011, 2020). We first recapitulate several bottlenecks associated with this scenario: 1) an adequate reservoir of residual planetesimals, 2) the conversion from distant residual planetesimals to LPCs, 3) a sustained supply of mostly-refractory cometary bodies over Gyr time scales, and 4) the orbital decay of the cometary nuclei, and their fragmentation and accretion onto the WDs. We briefly discuss some of these issues in the present context.

2.1. Residual planetesimal belts around WDs.

Since the observed properties of comets in the Solar System can be characterized in detail, their origin and evolution (Oort 1950) are often used as an analogue model and guide for the reservoirs of residual planetesimals around other stars including WDs and their main-sequence progenitors. A frequently applied minimum-mass solar-nebula (MMSN) model for the formation of the Solar System is based on the assumptions that major, dwarf, and minor planets are formed *in situ* with a maximum retention efficiency of heavy elements (Hayashi et al. 1985). Its extrapolation implies a mass $\sim 10^2 M_\oplus$ of planetesimals building blocks within a few tens of au in the solar nebula. Protoplanetary and debris disks with similar inventory and dimension appear to be prevalent among young stars (e.g., Andrews et al.

2018; Long et al. 2018, and references therein). The progenitors of currently observed WDs are generally more massive than the Sun with a mass distribution peaking at $1.5\text{--}2.5M_\odot$ (Hurley et al. 2000; Tremblay et al. 2016; Barrientos & Chanamé 2021). Since 1) exoplanets, especially multiple super-Earth systems are ubiquitous around FGK main-sequence stars and 2) the occurrence rate of gas giant planets increases with their host star's mass (Cumming et al. 2008; Howard et al. 2012; Petigura et al. 2013; Fabrycky et al. 2014), we assume that planet formation processes are robust (Ida & Lin 2004; Ida et al. 2013) and the initial seeding as well as subsequent dynamical evolution of residual planetesimals in the Solar System can be applied to planets and their building blocks around WDs and their progenitors.

During the advanced stages of their growth, the emerging proto ice and gas giant planets in the Solar System scattered nearby planetesimals into the Kuiper belt (with semi-major axes, $30 \text{ au} \lesssim a \lesssim 10^3 \text{ au}$) and inner ($a \sim 10^{3-4} \text{ au}$) and outer ($a \sim 10^{4-5} \text{ au}$) Oort cloud, respectively (Oort 1950; Zhou & Lin 2007; Dones et al. 2015). As their natal disks deplete, eccentric planets' secular resonances sweep through the planet forming region, exciting the eccentricities of residual planetesimals, efficiently clearing them from the planetary domain (including the asteroids' main belt), and launching them to much larger (or smaller) semi-major axes (Nagasawa et al. 2005; Zheng et al. 2017a,b). These planetesimal scattering processes also drive the planets to migrate (Fernández & Ip 1984). After the disk is severely depleted, the dynamical evolution of residual planetesimals continues to be influenced by the secular evolution and stability of their hosting planetary system (Tsiganis et al. 2005; Gomes et al. 2005).

Since most stars, including the Sun, are formed in dense stellar clusters that become dispersed (under the combined contribution from the stellar relaxation and Galactic tidal field) within ~ 0.1 Gyr (Adams 2010), they withstand close encounters with stellar neighbors, which also lead to modest semi-major axis changes and a nearly uniform eccentricity and inclination distribution for the planetesimals in the inner Oort cloud (Veras et al. 2020). A significant fraction of more distant residual planetesimals become detached from their host stars (Portegies Zwart et al. 2018).

During the Sun’s main-sequence evolution, it has been repeatedly bombarded by a few short-period (SPCs with orbital periods ≤ 200 yr, e.g., Halley) and long-period (LPCs with orbital periods ≥ 200 yr, e.g., Hale-Bopp) comets each year. The SPCs originate from the Kuiper belt which stores a total of $\lesssim 10^{-3} M_{\oplus}$ dwarf planets and residual planetesimals (Fraser et al. 2014) and it is being continually sculpted by perturbation from the gas and ice giants (Duncan et al. 1987, 1988). The LPCs are drawn from the scattered disk and Oort cloud. Under the perturbation of Galactic tides and passing giant molecular clouds (GMCs) and stars, residual planetesimals in this region generally preserve their large semi-major axes (Spurzem et al. 2009; Punzo et al. 2014; Veras et al. 2020) while their eccentricities are excited over the host stars’ multi-Gyr main-sequence evolution (see Section 2.2).

The Sun is half way through its 10 Gyr main-sequence evolution. During a brief interval (~ 1 Myr) on the asymptotic-giant branch and planetary-nebula phase, the progenitors of WDs out-shined the Sun by 3–5 orders and lost a major fraction of their original mass (Hurley et al. 2000). Modest size (up to 10 km in radius) asteroids originally located in the current main belt region ($\sim 2 - 4$ au) are either engulfed by the greatly expanded stellar envelope or downsized through sublimation. Kuiper belt objects (KBOs, initially located at 30 au to a few 10^2 au) are de-volatilized and their orbital semi-major axes undergo adiabatic expansion. Sub-km KBOs also migrate due to the Yarkovsky and the coupled YORP effects (Veras et al. 2019). Neither the composition nor the orbits of residual planetesimals in the outer Kuiper belt and inner Oort cloud (originally at or beyond a few 10^2 au) are altered largely by host stars’ intensified radiative flux. In response to the stellar mass loss during the subsequent planetary nebula phase, most planets and residual planetesimals with initial $a \lesssim 10^3$ au are retained by doubling their semi-major axes without changing their eccentricity (Debes & Sigurdsson 2002; Adams et al. 2013). However, more distant planetesimals with initial $a \gtrsim 10^3$ au are either

marginally retained with high eccentricities or released from the host stars’ gravitational confine (Veras et al. 2011; Rafikov 2018). Depending on the progenitors’ initial mass and planetesimals’ eccentricity and distribution, the region beyond $\sim 10^4$ au in recently emerged (young WDs may be sparsely populated with a precipitous drop-off in their density distribution).

The residual planetesimals around mature WDs continue to be perturbed by accompanied planets, Galactic tides, and passing GMCs and stars. But, their overall kinematic distribution evolves slowly on time scales longer than the Gyr age of their WD hosts. With these considerations, we assume that there is a population of residual planetesimals with asymptotic semi-major axes $a \lesssim 10^4$ au (equivalent to the region in the Solar System’s Kuiper belt and Oort cloud) around WDs. In order for these objects to reach the tidal radius of their WD hosts, they must acquire nearly parabolic orbits in which eccentricity $e = 1 - \epsilon$ with $\epsilon \lesssim 10^{-6}$.

2.2. Excitation of nearly parabolic orbits

In the outskirts of the Solar System, secular torque from Galactic tides and passing GMCs and stars leads to changes in these residual planetesimals’ angular momentum, excitation of their eccentricity Δe , and randomization of their inclination with much smaller fractional changes in their energy $\Delta E/E$ and semi-major axes $\Delta a/a$ (Heisler & Tremaine 1986). Consequently, their pericenter distances q diffuse towards the surfaces of their host stars with a nearly uniform inclination distribution (Wiegert & Tremaine 1999; Boe et al. 2019). Due to the host stars’ gravity, residual planetesimals with modest a (comparable to that in the Kuiper belt and inner Oort cloud) suffer limited fractional changes in their eccentricities $\Delta e/e$ and pericenter distances $\Delta q/q$ per orbit. A flux of residual planetesimals is continually fed to the proximity of planet-free host stars as LPCs. Since the strength of external perturbation relative to host stars’ gravity is an increasing function of a , many of the injected LPCs originated from the outer region where most of the residual planetesimals are populated (with $a \sim$ a few 10^3 au).

However, rich populations of residual planetesimals at Oort cloud distances is synonymous with not only ample supplies of planet-building blocks but also the omnipresence of giant-planet scatterers (Section 2.1). Around stars with giant planets at locations similar to those in the Solar System, the contraction of planetesimals’ q is temporarily interrupted by planets’ perturbation just exterior to their orbits (Fernández & Ip 1981). The giant planets’ gravity also imparts changes in the energy and angular momentum to the planetesimals and increases

in their a (Levison et al. 2006). With sufficiently large apo-center distances ($\gtrsim 10^4$ au) where the stellar gravity is relatively weak, Galactic tides and passing stars as well as GMCs induce the residual planetesimals to undergo large incremental $\Delta q/q$. These persistent changes allow a fraction of them to cross the giant planets' orbital barrier and be transformed into Sun-grazing LPCs (Hills 1981; Kaib & Quinn 2009).

During the Sun's lifespan, these competing effects cause about half of residual planetesimals population to be lost to the interstellar space and a smaller fraction to be injected into the inner Solar System (Hanse et al. 2017). With a total estimated population $N_{\text{rp}} \sim 10^{12}$ of residual planetesimals in the outer Oort cloud, this scenario can account for the observed infusion rate $\dot{n}_{\text{LPC}} \sim$ a few events per year (Everhart 1967; Francis 2005; Neslušan 2007; Kaib & Quinn 2009). The inner Oort cloud replenishes the outer Oort cloud with residual planetesimals (Hills 1981). Although a much larger population of residual planetesimals has been hypothesized for the inner Oort cloud (Fernández 1997; Levison et al. 2001), it does not directly source LPCs such that there has not been any observational constraints on its inventory. From the average mass ($M_{\text{LPC}} \sim 4 \times 10^{13}$ kg) and size distribution (Weissman & Levison 1997; Meech et al. 2004) of individual LPCs, the corresponding mass flux is $\dot{M}_{\text{LPC}} \sim M_{\text{LPC}} \dot{n}_{\text{LPC}} \sim 10^7$ kg s^{-1} and the equivalent total mass of this residual planetesimals in the outer Oort cloud is $M_{\text{rp}} = N_{\text{rp}} M_{\text{LPC}} \sim 2 - 7 M_{\oplus}$ (Weissman 1983; Weissman & Levison 1997). Uncertainties in these mass estimates are of order unity. Recent PanSTARR survey confirms the extrapolated existence of a rich population of residual planetesimals with uniform inclination distribution, random orbital orientations, and comparable total mass in the outer Oort cloud (Boe et al. 2019).

Around other planet-bearing stars, including WDs, the transition radii between SPCs and LPCs and between inner and outer Oort clouds are smaller for more compact or less massive planetary systems or in more dense stellar environments (Fernández 1997). On Gyr time scales, residual planetesimals with $a \sim 10^{3-4}$ au can continually feed their host stars at rates similar to \dot{n}_{LPC} in the Solar System whether or not they have accompanying giant planets. The magnitude of \dot{M}_{LPC} is comparable to or slightly larger than those inferred for the WDs' accretion ($\dot{M}_{\text{WD}} \sim 10^5 - 10^6$ kg s^{-1}) of refractory elements (Manser et al. 2019; Chen et al. 2019). In contrast to those around the Sun, the LPCs around WDs may have lost their volatile content during the red giant phase. Over the multi-Gyr age of typical WDs, the integrated amount of mostly refractory elements accreted

onto them, $M_{\text{Z}} \sim 0.01 - 0.1 M_{\oplus}$, is a small fraction of the present-day total mass estimated for the LPCs (Boe et al. 2019) and residual planetesimals (M_{rp}) in the Oort cloud but larger than the total mass in asteroids' main belt and KBOs in the Solar System. In terms of the mass budget, the outlying LPCs appear to be the most likely candidates for the parent bodies of WDs' dusty disks and heavy elemental contaminants.

LPCs in the Solar System have an average size of a few km with a steep fall off in their size frequency distribution (Meech et al. 2004; Boe et al. 2019). *In situ* formation of larger planetesimals beyond the Kuiper belt is likely to limit the high end of their mass function due to the density fall off of their building block material (Morbidelli et al. 2021). While the large (100–1000 km-size) dwarf planets may dominate the total mass of the scattered population in the Kuiper belt (Fraser et al. 2014), the probability and resultant distribution of their asymptotic apo-center distances decline with their semi-major axes expansion factor. We expect that the number density of large residual planetesimals at 10^{3-4} au from their host stars may be so sparse that their rare transition into LPCs is negligible.

Based on the extrapolation of these observed properties for the Solar System LPCs to the parent bodies of debris disks around and heavy elements accreted onto the WDs, we assume that, they have an average size $r \sim 10$ km, $a \sim 10^{3-4}$ au, $q \sim 0.1 R_{\odot} - R_{\odot}$, random distributions in inclination, pericenter argument, and ascending node. We choose this range of a for LPCs on the bases: 1) a significant fraction of the residual planetesimals at this location is retained despite the mass loss during the red giant phase; 2) the external perturbation is sufficiently intense for the residual planetesimals to diffuse towards the stellar surface over Gyr time scales; 3) although giant planets at a few au, if present, would temporarily interrupt the decline in q , their barrier can be effectively bypassed through dynamical channels similar to those in the Solar System (i.e., Kaib & Quinn 2009). The following sections examine the tidal downsizing and orbital evolution of these parent bodies and their fragments.

3. TIDAL DOWNSIZING OF RESIDUAL PLANETARY BODIES

There are two potential reservoirs for the parent bodies of the debris disks and WD pollutants. These parent bodies may originate from the residual planetesimals either at a location interior to some retained giant planets (similar to the asteroids) or far from their host stars (analogous to the long-period comets, LPCs, see Section 2). Both the asteroid and the LPC scenarios assume the

accreted heavy elements are mostly byproducts of collisions, PR drag, orbital decay, planetary scattering, and tidal disruption (e.g., [Chen et al. 2019](#); [Veras et al. 2014](#); [Malamud et al. 2021](#)). The main differences between the dynamical properties of the parent bodies in these two models are: 1) the semi-major axis, 2) inclination, and 3) eccentricity distribution. Here, we adopt a general model for the fragmentation of parent bodies with diverse structural properties and material strengths.

3.1. Condition for tidal fragmentation

As perturbed by the combination of Galactic tides, passing stars, residual giant planets, and stellar components, a fraction of residual asteroids and comets are continually scattered into nearly parabolic orbits with pericenters that are in close proximity to their host WD ([Kaib & Quinn 2009](#); [Kratter & Perets 2012](#); [Veras 2016](#); [Hamers & Portegies Zwart 2016](#)). They undergo tidal disruption when the pericenter distances are reduced below some critical values, where tidal forces imposed by the WD overwhelm the gravitational forces and material strength that hold these objects together and may disrupt them.

The tidal disruption limiting distance of an initially spherical, non-spinning, viscous fluid object is ([Sridhar & Tremaine 1992](#))

$$d_{\text{gra}} = 1.05 \left(\frac{M_{\star}}{\rho} \right)^{1/3}, \quad (1)$$

where ρ is the bulk density of the object and M_{\star} is the mass of the WD. d_{gra} is appropriate to predict the tidal disruption distance for objects in the gravity-dominated regime, such as gas giants, super-Earths with molten interiors, and minor and dwarf planets with sizes $\gtrsim 10$ km. While for small objects in the strength-dominated regime, their intrinsic material shear and tensile strengths can prevent tidal disruption within this limit and determine their survivability ([Zhang & Lin 2020](#); [Zhang & Michel 2020](#)).

To reflect the material characteristics, we follow the pioneer work of [Holsapple & Michel \(2008\)](#) and use the elastic-plastic continuum theory for solid and granular material to estimate the tidal disruption limit of small bodies. For geological materials, the tensile and shear strengths depend strongly on the loading conditions (i.e., circumambient pressures; [Holsapple 2007](#)). The Drucker-Prager failure criterion that is appropriate for a large class of solid and granular geological material is applied to determine the failure of such objects,

$$\sqrt{J_2} \leq k - sI_1, \quad (2)$$

where I_1 is the first invariant of the Cauchy stress tensor, and J_2 is the second invariant of the deviatoric stress

tensor, which can be written in terms of the principal stresses, $(\sigma_1, \sigma_2, \sigma_3)$, as $I_1 = \sigma_1 + \sigma_2 + \sigma_3$, $J_2 = [(\sigma_1 - \sigma_2)^2 + (\sigma_2 - \sigma_3)^2 + (\sigma_3 - \sigma_1)^2]/6$. The material constants s and k can be expressed as a function of the commonly-used friction angle, ϕ , and cohesive strength C (which represents the shear strength at zero pressure),

$$s = \frac{2 \sin \phi}{\sqrt{3}(3 - \sin \phi)}, \quad k = \frac{6C \cos \phi}{\sqrt{3}(3 - \sin \phi)}. \quad (3)$$

The structure of an object fails when its internal stress state violates this criterion.

Subject to the self gravity and the host WD's tidal effect, the volume-averaged normal stress components of a non-spinning spherical object for an encounter at a distance d with respect to the WD's mass center are given as

$$\begin{aligned} \bar{\sigma}_x &= \left[-\frac{4}{3}\pi\rho^2G + \frac{8\pi}{3}G\rho\rho_{\star} \left(\frac{d}{R_{\star}} \right)^{-3} \right] \frac{r^2}{5}, \\ \bar{\sigma}_y &= \left[-\frac{4}{3}\pi\rho^2G - \frac{4\pi}{3}G\rho\rho_{\star} \left(\frac{d}{R_{\star}} \right)^{-3} \right] \frac{r^2}{5}, \\ \bar{\sigma}_z &= \left[-\frac{4}{3}\pi\rho^2G - \frac{4\pi}{3}G\rho\rho_{\star} \left(\frac{d}{R_{\star}} \right)^{-3} \right] \frac{r^2}{5}, \end{aligned} \quad (4)$$

where ρ and r are the bulk density and radius of the object, and ρ_{\star} and R_{\star} are the bulk density and radius of the WD, respectively. G is the gravitational constant. These stress components are expressed in a right-hand Cartesian coordinate system originating at the object's mass center, where x -axis is towards the WD center and z -axis is perpendicular to the orbital plane. Since the averaged shear stress components are exactly zero in this coordinate system, we have the averaged principle stresses $\bar{\sigma}_1 = \bar{\sigma}_x$, $\bar{\sigma}_2 = \bar{\sigma}_y$, $\bar{\sigma}_3 = \bar{\sigma}_z$.

By substituting the stresses into the failure criterion (Eq. (2)), the tidal disruption limit for an object in the strength-dominated regime is given as

$$d_{\text{str}} = \left(\frac{\sqrt{3}}{4\pi} \right)^{1/3} \left(\frac{5k}{4\pi G r^2 \rho^2} + s \right)^{-1/3} \left(\frac{M_{\star}}{\rho} \right)^{1/3}, \quad (5)$$

which generally decreases with either a larger friction angle ϕ or stronger cohesion C . This limit is much smaller than the limit in the gravity-dominated regime, e.g., even for low-strength material with $\phi = 25^\circ$ ¹ and $C = 0$ Pa, $d_{\text{str}} = 0.9(M_s/\rho)^{1/3} < d_{\text{gra}}$. Material strength in small bodies provides a stabilizing effect against the host WD's tidal perturbation.

If C is relatively large, this equation degenerates into

$$d_{\text{str}} = \left(\frac{\sqrt{3}Gr^2\rho M_{\star}}{5k} \right)^{1/3}, \quad (6)$$

¹ The friction angle of geological materials commonly ranges from 25° to 50° (e.g., [Bareither et al. 2008](#)).

which has the same format as the tidal disruption limit in the strength-dominated regime derived by Brown et al. (2017, see their Eq. (29)), but with slightly different coefficients. The study of Brown et al. (2017) considers a pure tensile failure mode and neglects the internal pressure and shear stresses, while Eq. (5) is derived from the global stress analyses and is applicable for various failure modes and strength levels.

3.2. Maximum survivor size at different pericenter distances

According to Eq. (5), d_{str} is size-dependent when the object's cohesive strength $C > 0$ Pa. In this case, the material strength and size of an object determine its integrity in the proximity of a WD. With a given amount of cohesion, the maximum possible size of the survivors $r_{\text{max,sur}}$ that can maintain their integrity at a certain pericenter distance q can be estimated by this equation.

WD Cooling Age: 4 Gyr 1.5 Gyr 0.5 Gyr 0.1 Gyr 20 Myr
 Sublimation Distance: $0.05R_{\odot}$ $0.1R_{\odot}$ $0.2R_{\odot}$ $0.5R_{\odot}$ $1R_{\odot}$

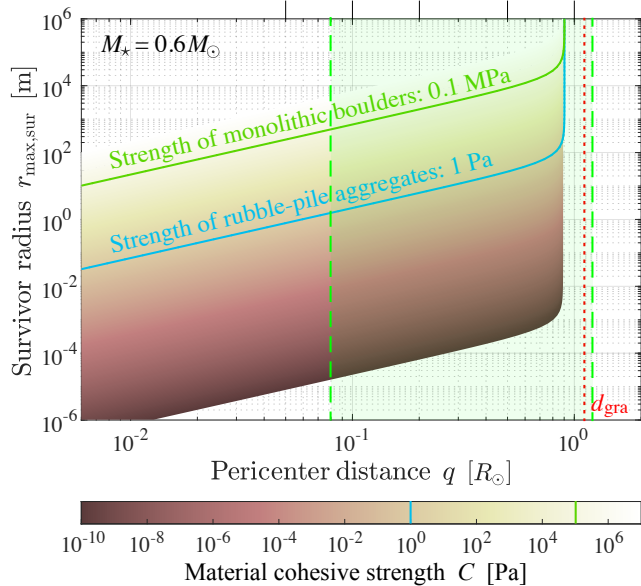


Figure 2. Maximum survivor size at different pericenter distances. The colorbar represents the material strength magnitude. The distances for silicate sublimation at various WD cooling ages are indicated on the top (following Eq. (1) given in Rafikov 2011). The greenish area in between the two given vertical dashed lines represent the radius range of tidal debris disks around WDs deduced from observations (e.g., von Hippel et al. 2007; Xu et al. 2017) and theoretical analyses (e.g., Rafikov & Garmilla 2012). The red vertical dotted line denotes the tidal disruption limit at the gravity-dominated regime. The survivor sizes for material strength of 1 Pa and 0.1 MPa are highlighted by the blue and green solid curves, respectively.

Figure 2 shows the maximum possible size of debris around a WD with a typical mass $M_{\star} = 0.6M_{\odot}$ at different pericenter distances for a range of material cohesive strength. A bulk density of 3000 kg/m^3 and a friction angle of 30° (analogue to the properties of Solar System S-type asteroids; Carry 2012; Zhang et al. 2017) are used for these estimates. Since $d_{\text{str}} \propto M_{\star}^{1/3}$, this results can be scaled to different WD mass M_{\star} .

Our evaluation of the tidal disruption limit d_{str} is consistent with the observed radius range of tidal debris disks around WDs (i.e., the greenish area in Fig. 2). Within this range, grains and boulders that constitute the approached rubble-pile object are separated into individual debris if their connections are cohesionless. Some meter-sized aggregates could survive if the van der Waals cohesive forces between fine grains (Scheeres et al. 2010; Zhang et al. 2018) could provide cohesive strength on the order of 1 Pa. With the typical material cohesive strength of meteorites (i.e., 0.1–10 MPa; Pohl & Britt 2020), monolithic bodies with sizes up to 10 km can remain intact. It is therefore appropriate to assume that the typical size of macroscopic tidal debris orbiting WDs ranges from ~ 1 cm to ~ 10 km. In the following section, we will investigate the effect of WD magnetic fields on objects within this size range.

4. ORBITAL MIGRATION AND CIRCULARIZATION BY ALFVÉN-WAVE DRAG

After the tidal disruption, the fragments follow similar paths as their parent bodies. Although some azimuthal dispersion occurs after a few hundred orbital periods for the debris of parent bodies with semi-major axes similar to the main belt asteroids (Malamud & Perets 2020), it takes much longer for the distant LPCs. In an attempt to investigate the fragments' circularization process, we consider their interaction with the magnetic fields of their host WDs.

4.1. Orbital migration of tidal debris

When an object moves through a magnetized flowing plasma, it induces an impulse (i.e., Alfvén wave) traveling along the magnetic field that generates significant drag effects on its motion (Drell et al. 1965). Here we consider a tidal fragment orbiting a magnetic WD on a highly eccentric orbit with a pericenter within the tidal disruption limit of the WD. The radius and density of this fragment are denoted as r and ρ , respectively, and thus the mass $m = 4\pi r^3 \rho / 3$ (assumed to be spherical).

Assuming the WD has a surface magnetic flux density B_{\star} , for an object at a distance d from the WD, where the flux density $B = B_{\star} (R_{\star}/d)^3$, the Alfvén wave is emitted along a wing with a power (Drell et al. 1965; Neubauer

1980)

$$P \simeq \pi U^2 / R_{\text{wing}}, \quad (7)$$

where $U = rvB$ is the electric potential of the electric field induced by this object across its radius r (with an orbital speed v), and $R_{\text{wing}} = \mu_0 \bar{v}_A = \mu_0 v_A \sqrt{1 + M_A^2 + 2M_A \sin \theta}$ is the effective resistance provided by the surrounding plasma. The permeability of free space $\mu_0 = 4\pi \times 10^{-7} \text{ N A}^{-2}$. The Alfvén speed, $v_A = B / \sqrt{\mu_0 \rho_g}$ (where ρ_g is the ionized gas mass density), and the Alfvén Mach number $M_A = v / v_A$. We neglect the spin of the WD such that v is assumed to be the orbital motion of the object.² θ is the deviation of the object’s velocity from being perpendicular to the magnetic field.

4.1.1. Energy dissipation rate

Interacting with the Alfvén-wave drag, the body’s kinetic energy per unit mass is dissipated at a rate

$$\frac{1}{2} \frac{dv^2}{dt} = -\frac{P}{m} = -\frac{3v^2 B^2}{4\rho r \mu_0 \bar{v}_A} \quad (8)$$

This Alfvén-wing drag force has a similar, but not identical, dependence on the stellar magnetic field as the diamagnetic planetary debris model, which is based on the assumption of a back reaction by the distorted field lines wrapped around the moving object (King 1993; Hogg et al. 2021). These two assumptions lead to a magnitude difference in the drag force by a factor v / \bar{v}_A . Since $\bar{v}_A \propto B$, this factor can depart from unity in the limit of modest B_* .

As the magnetic flux density B decay rapidly with a larger distance d , the orbital modifications caused by this mechanism is just effective around the pericenter, where the distance $d = q = a(1 - e)$, where e and a are the orbital eccentricity and semi-major axis, respectively. The total energy change during one passage can be estimated by

$$\Delta E = \frac{1}{2} \frac{dv^2}{dt} \Delta t_{\text{peri}}. \quad (9)$$

The duration of the pericenter passage $\Delta t_{\text{peri}} = \alpha / \Omega$, where the angular speed at pericenter $\Omega = \sqrt{GM_* a(1 - e^2)} / a^2(1 - e)^2$, and α is the pericenter passage angle within which the Alfvén-wave drag takes effect. Given that $1 - e = \varepsilon \ll 1$, and $\Omega = \sqrt{GM_*} / a^3 \varepsilon^3$,

² With the model parameters we adopt below (i.e., $q = 10^{-3} a$ and $M_* = 0.6M_\odot$; see Table 1), the orbital frequency at the pericenter corresponds to a period of $2\pi(2q^3/GM_*)^{1/2} \sim 600$ s, which is much shorter than the spin periods of most WDs (e.g., Koester et al. 1998; Hermes et al. 2017).

the energy change can be given as

$$\Delta E = -\frac{3\alpha v^2 B_*^2 R_*^6}{4\rho r \mu_0 \bar{v}_A a^5 \varepsilon^5} \sqrt{\frac{a\varepsilon}{GM_*}}. \quad (10)$$

Substituting v with the speed at perihelion $v_{\text{peri}} = \sqrt{GM_*(2 - \varepsilon)} / a\varepsilon \approx \sqrt{2GM_*} / a\varepsilon$,

$$\Delta E = -\frac{3\alpha B_*^2 R_*^6}{2\rho r \mu_0 \bar{v}_A a^5 \varepsilon^5} \sqrt{\frac{GM_*}{a\varepsilon}}. \quad (11)$$

With the total specific orbital energy $E = -GM_*/2a$, the energy change rate per orbit can be estimated by

$$\frac{\Delta E}{E} = \frac{3\alpha B_*^2 R_*^6}{\rho r \mu_0 \bar{v}_A a^4 \varepsilon^5 GM_*} \sqrt{\frac{GM_*}{a\varepsilon}}. \quad (12)$$

4.1.2. Semi-major axis change rate

The energy dissipation would lead to semi-major axis decay, which can be estimated by

$$\frac{\Delta a}{a} = -\frac{\Delta E}{E} \quad (13)$$

4.1.3. Eccentricity change rate

With the assumption that this effect is only effective near the pericenter, the pericenter distance q can be regarded as a constant, $q = q_0$, and therefore

$$\Delta e = -(1 - e) \frac{\Delta E}{E}, \quad (14)$$

4.2. Orbital circularization timescale

Now we investigate the long-term orbital migration of an object due to the Alfvén-wave drag effect. The initial orbital semi-major axis and eccentricity are denoted as a_0 and e_0 , respectively. After n times pericenter approaches, the semi-major axis a_n is described as the following polynomial recursion format,

$$a_n = a_{n-1} + \Delta a_{n-1} = a_{n-1} - \lambda a_{n-1}^2, \quad (15)$$

where $\lambda = \Delta E_{n-1} / (E_{n-1} a_{n-1}) = \Delta E_0 / (E_0 a_0) = \text{constant}$.

The analytical solution of this recursion is given by

$$a_n = a_0 \mathbf{I} \mathbf{T}^n \mathbf{E}_0, \quad (16)$$

where $\mathbf{T} \in \mathbb{Z}^{2^n \times 2^n}$ is the upper triangular transfer matrix with elements

$$T_{jk} = (-1)^{k-j} \binom{k}{k-j}. \quad (17)$$

The vector $\mathbf{I} = [\delta_{i1}]_{i=1,2,\dots,2^n} \in \mathbb{Z}^{1 \times 2^n}$, where δ_{i1} is the Kronecker symbol. The vector $\mathbf{E}_0 = [(\Delta E_0 / E_0)^{i-1}]_{i=1,2,\dots,2^n} \in \mathbb{Z}^{2^n \times 1}$.

The semi-major axis after n encounters, a_n , can be expressed more concisely in such a form,

$$a_n = \sum_{i=0}^{2^n-1} (-1)^i a_0 P_i(n) \left(\frac{\Delta E_0}{E_0} \right)^i, \quad (18)$$

where $P_i(n)$ is the i -th degree polynomials of n .

Given that the corresponding orbital eccentricity $e_n = 1 - q/a_n$, the number of orbits required to reduce the eccentricity to 0.1, $n_{e=0.1}$, can be obtained by solving $a_{n_{e=0.1}} = 10a_0(1 - e_0)/9$. By substituting Eq. (18) into the above equation, we find that, approximately, $n_{e=0.1}$ is proportional to $(\Delta E_0/E_0)^{-1}$ and slowly decreases with a larger e_0 for a given pericenter distance.

The total timescale is then given as (assuming the starting point is the apocenter)

$$\Delta T_{e=0.1} = \pi \sqrt{\frac{a_0^3}{GM_\star}} + \frac{2\pi}{\sqrt{GM_\star}} \sum_{i=1}^{n_{e=0.1}} a_i^{1.5}. \quad (19)$$

In the case where $n_{e=0.1} \gg 1$, $\Delta T_{e=0.1}$ is proportional to the total number of orbits $n_{e=0.5}$, i.e.,

$$\Delta T_{e=0.1} \propto \sqrt{\frac{a_0^3}{GM_\star}} \left(\frac{\Delta E_0}{E_0} \right)^{-1} = \frac{\rho r \mu_0 \bar{v}_A q_0^{5.5} \sqrt{a_0}}{3\alpha B_\star^2 R_\star^6}. \quad (20)$$

In another extreme where the orbital circularization is fast and $n_{e=0.1}$ is small, $\Delta T_{e=0.1}$ mainly depends on the initial orbital semi-major axis, i.e.,

$$\Delta T_{e=0.1} \propto \sqrt{\frac{a_0^3}{GM_\star}}. \quad (21)$$

Therefore, in general, we have

$$\Delta T_{e=0.1} \propto \sqrt{\frac{a_0^3}{GM_\star}} \left(\frac{\Delta E_0}{E_0} \right)^{-1/\beta}, \quad (22)$$

where $\beta \gtrsim 1 \in \mathbb{R}$ and depends on the circularization efficiency. When the efficiency is low, $\beta \rightarrow 1$ and Eq. (22) degenerates into Eq. (20). On the other hand, if the object's orbit can be circularized in a few pericenter approaches, $\beta \rightarrow \infty$ and Eq. (22) degenerates into Eq. (21).

To give some quantitative estimates on the timescale, we consider orbital migration of an object around a typical WD, whose $M_\star = 0.6M_\odot$, $R_\star \approx 0.0125R_\odot$ ³. Assuming that $B_\star = 100$ T (i.e., 10^6 G in cgs units),

³ The WD radius is estimated by $R_\star = 0.0127R_\odot (M_\star/M_\odot)^{-1/3} [1 - 0.607(M_\star/M_\odot)^{4/3}]^{1/2}$ (Veras & Heng 2020).

Table 1. Parameter setup in the numerical simulations for testing the effect of Alfvén-wave drag.

Symbol	Value	Meaning
M_\star	$0.6 M_\odot$	WD mass
R_\star	$0.0125 R_\odot$	WD radius
B_\star	100 T (or 10^6 G)	Magnetic field at the surface of WD
\bar{v}_A	3×10^7 m/s	Scaled Alfvén speed
r	$0.01\text{--}10^4$ m	Debris radius
a_0	$1\text{--}10^4$ au	Debris semi-major axis
q_0	0.001–0.002 au	Debris periastron distance
ε_0	$10^{-7}\text{--}10^{-3}$	$1 - e_0$
ρ	3000 kg/m ³	Debris bulk density
α	$\pi/2.24$	Empirical pericenter passage angle

$\rho \sim 3000$ kg/m³, $r = 1$ m, $\bar{v}_A = 3 \times 10^7$ m/s⁴, $a_0 = 10$ au, $\varepsilon_0 = 10^{-4}$ ⁵, and α is set to a constant $\pi/2.24$ by calibration with numerical simulations in Section 5, the energy dissipation rate $\Delta E/E \sim 0.027$. In this particular case, the object's orbital eccentricity decays to 0.1 after $\sim 306,000$ orbits, which corresponds to a timescale about 2.7 kyr. In general, the timescale scales as $2.7(r/1 \text{ m})(a_0/10 \text{ au})^{0.5}$ kyr approximately, suggesting that the Alfvén-wave drag is an efficient mechanism for the orbital circularization of sub-100 km-sized planetary remnants around magnetic WDs.

With these model parameters, $v/\bar{v}_A \sim 0.032 - 0.043$ such that the Alfvén wave drag force we used here is an order of magnitude smaller than that adopted by Hogg et al. (2021) for the diamagnetic planetary debris model. Despite our conservative choices, the high efficiency of circularization by this process appears to be robust. The measured B_\star for WDs has a wide range (10^{3-9} G; Ferrario et al. 2015). Since the Alfvén speed $v_A \propto B$, $\Delta E/E \propto B$ and $dv/dt \propto B$ (Eqs. (12) & (23)). The circularization timescale is proportional to B_\star^{-1} . Nevertheless, tidal fragments of km-sized LPCs (with $a_0 \sim 10^3$ au) can be circularized in $\lesssim 1$ Gyr around weakly magnetized WDs (with kilogauss B_\star).

5. NUMERICAL SIMULATIONS

In this section, we validate the analytical estimation presented in Section 4 by numerical simulations. We use

⁴ The Alfvén wave drag is stronger with a smaller \bar{v}_A . For a conservative estimate, we adopt a constant large value for \bar{v}_A in this study. The actual value of \bar{v}_A depends on the magnetic flux density, the surrounding ionized gas mass density, the orbital motion of the encountered object, and the magnetic field direction, which are poorly constrained based on current observations and whose effects will be examined for future studies.

⁵ So the perihelion distance $q \approx 0.2R_\odot$, which is within the tidal disruption limit of most WDs; see Fig. 2.

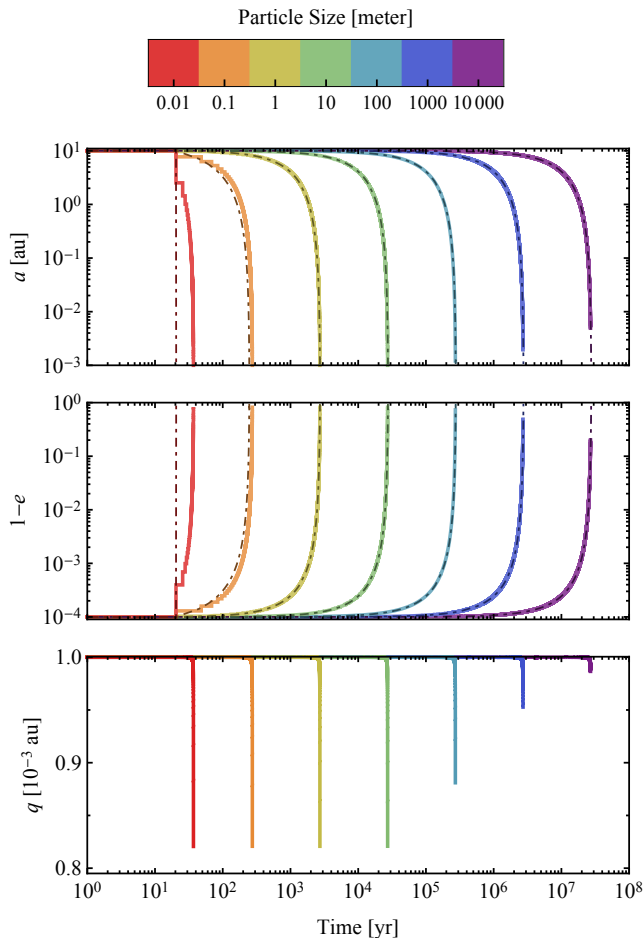


Figure 3. Orbital circularization of different sized fragments caused by the Alfvén-wave drag from an initial orbit with $a_0 = 10$ au and $e_0 = 0.9999$. Evolution of orbital semi-major axis a , eccentricity represented by $1 - e$, and the periastron distance q are plotted. Lines are color-coded with sizes of fragments. Solid lines are results from numerical integrations, while dot-dashed lines are analytic estimations (Section 4.2).

the the IAS15 integrator (Rein & Spiegel 2015) within the REBOUND package (Rein & Liu 2012) to numerically integrate orbits of the tidal debris and determine the orbital migration timescales on various initial orbits. The debris is treated as a test particle, which is subject to the Alfvén-wave drag in addition to the gravitational force from the host. The Alfvén-wave drag is opposite to the particle’s motion and the magnitude of deceleration at a distance d from the WD can be characterized by

$$\frac{dv}{dt} = -\frac{3vB_\star^2 R_\star^6}{4\rho r d^6 \mu_0 \bar{v}_A}. \quad (23)$$

We consider a typical WD with a mass $M_\star = 0.6M_\odot$ and a radius $R_\star = 0.0125R_\odot$. Other parameters are summarized in Table 1. For all cases, we start numerical

integrations from the apocenter of an initial orbit with a semi-major axis a_0 and an eccentricity e_0 .

In the first test, we adopt the initial orbit with $a_0 = 10$ au and $e_0 = 0.9999$ to examine the effect of debris size and make comparisons with the analytic approximation in Section 4. Figure 3 shows the orbital evolution of the tidal debris with sizes ranging from 0.01 m to 10 km. The Alfvén-wave drag is only effective at the proximity of the WD as $dv/dt \sim -d^{-6}$, so it gets intensified rapidly near the periastron and is negligible for the rest of the time. In addition, since the magnetic drag force is inversely proportional to the size of debris, a smaller fragment feels a much stronger drag effect than a bigger one. As a result, a small fragment ($r = 0.01$ m) could lose a significant fraction of its orbital energy, e.g., $\Delta E/E \gtrsim 1/2$, and its orbit is rapidly circularized within a few periastron passages. In Figure 3, the staircase-like variations of a and $1 - e$ are evident for the smallest fragment ($r = 0.01$ m) during the first few orbits. We stop the numerical integration when a becomes smaller than 10^{-3} au, which equals to q_0 , the initial periastron distance. Further orbital shrinkage would require proper treatment of general relativity, which is not the focus of this paper. For fragments with radii larger than 100 m, our numerical integrations end at slightly larger semi-major axes due to time steps being extremely small.

As noted in Section 4, the circularization timescale is proportional to the size of debris. We overplot the analytical estimation for each sizes in thin dot-dashed lines in the a and $1 - e$ plots for comparison. The numerical results show good consistency except for the smallest size ($r = 0.01$ m) where the analytical result underestimates the circularization timescale because the orbital circularization is fast and the timescale is determined by initial orbital period (see Eq. (21)). Numerical results also suggest that, during the orbital circularization, the periastron distance remains almost unchanged in all cases, validating the assumption adopted for the analytical estimation (i.e., see Section 4.1.3).

We further explore the dependence of orbital circularization on the initial locations of debris for given fragment sizes ($r = 0.01$ m, $r = 10$ m and $r = 10$ km). Figure 4 presents the evolution of a and $1 - e$ as a function of time for each considered size of debris. We keep the periastron distance $q_0 = 10^{-3}$ au constant and vary the initial semi-major axis a_0 from 1 au to 10^4 au (in colored solid lines) except for one initial orbit with $a_0 = 10$ au and $q_0 = 2 \times 10^{-3}$ au (in black dashed line). For debris at size $r = 0.01$ m, the Alfvén-wave drag is so efficient that it can circularize the orbit of fragments from the Oort cloud after one passage with $q_0 = 10^{-3}$ au (consistent with the estimation of Eq. (21)). For debris at

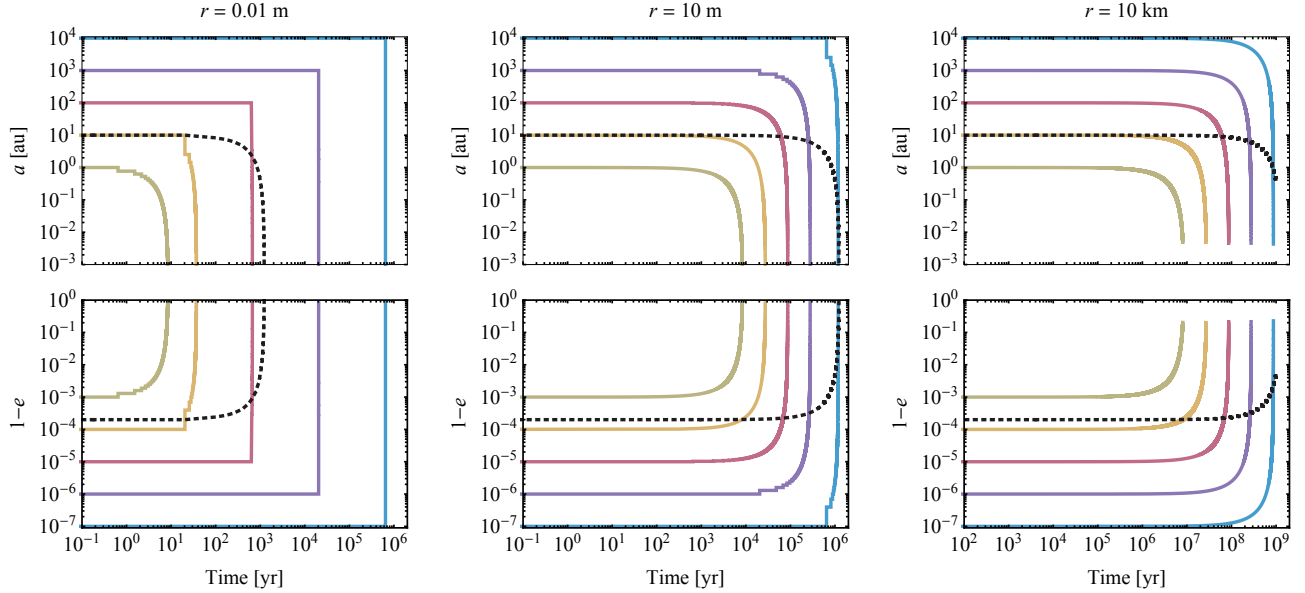


Figure 4. Orbital circularization of fragments with sizes at $r = 1$ cm (left column), $r = 10$ m (middle column) and $r = 10$ km (right column) caused by the Alfvén-wave drag. Evolution of orbital semi-major axis a , eccentricity represented by $1 - e$ are plotted. Colored solid lines are cases with an initial periastron distance $q_0 = 10^{-3}$ au, while black dashed lines are cases with an initial periastron distance $q_0 = 2 \times 10^{-3}$ au.

size $r = 10$ m and $r = 10$ km, the orbital circularization timescale is consistent with the analytical estimation given by Eq. (20), i.e., ~ 1 Myr for $r = 10$ m and ~ 1 Gyr for $r = 10$ km for debris from the Oort cloud.

Our analytical and numerical investigations reveal that the Alfvén drag-assisted circularization is a rapid and robust process that can completely circularize large residual planetesimals from the Oort cloud around magnetic WDs. The derived time scale is comparable to or shorter than other rapid circularization methods proposed by previous theoretical works that consider the effect of dust or gas drag of a pre-existing gaseous or massive compact disk (Grishin & Veras 2019; Malamud et al. 2021) or tidal migration of planetesimals with high internal viscosity (O’Connor & Lai 2020). Moreover, the Alfvén drag mechanism does not require the ram-pressure drag by hypothetical gaseous or debris disks or by tidal dissipation of bodies with molten interiors.

6. METAMORPHOSIS FROM LPCS TO CLOSE-IN FRAGMENTS

In Section 2, we adopted the assumption that WDs bear rich reservoirs of residual planetesimals at distances comparable to the Oort cloud. This population of residual planetesimals can sustain protracted injection of LPCs into their tidal disruption radius close to their host stars. When their pericenter distances are reduced below d_{gra} and d_{str} , the residual planetesimals are tidally disrupted (see Section 3). According to Fig. 2 and Eq. (5), at the pericenter distance $q = 10^{-3}$ au, the

maximum sizes of the surviving fragments $r_{\text{max,sur}}$ is ~ 1 m and ~ 10 km for LPCs with rubble-pile and monolithic structures, respectively. These fragments approximately follow the paths of their LPC parent bodies. Their orbits must be circularized before they can settle into debris disks interior to $d_{\text{gra}} (\sim R_{\odot})$. Such disks are commonly found around young ($< \text{Gyr}$ old) WDs with signatures of metal enrichment through recent accretion of refractory material (Mullally et al. 2007; Farihi et al. 2009; Farihi 2016; Manser et al. 2020). This requirement is challenging since the dynamical time scale for LPCs with $a \sim 10^{3-4}$ au is $P \sim 10^{5-6}$ yr. Around some recently emerged WDs (with ages of $\lesssim 10^8$ yr), the LPCs’ fragments must be effectively circularized within $\sim 10^{2-3}$ orbits.

As discussed in the beginning of this paper (e.g., see Fig. 1), one efficient mechanism to transform the residual planetesimals’ nearly parabolic to nearly circular orbits is through their interaction with their magnetized host WDs during their pericenter passages. Our analytic and numerical results (Sections 4 & 5) show that the circularization time scale $\Delta T_{e=0.1} \propto q_0^{5.5}$ for a constant a_0 (Eq. (20)). We consider modal parameters for LPCs that enters inside the tidal disruption radius during their pericenter approach. For a fiducial residual planetesimal with $r = 10$ km, $q = 10^{-3}$ au, and $a = 10^4$ au, $\Delta T_{e=0.1} < 1$ Gyr. The results in Section 5 show rapid decreases in a and e but little change in q . For the same pericenter distance, $\Delta T_{e=0.1} \propto ra^{1/2}$, which decreases during the tidal downsizing and orbital de-

cay processes. Therefore, the timescale for typical LPCs to circularize their orbits is a small fraction of that for them to be transformed from residual planetesimals in the Oort cloud.

After the eccentricity of individual fragments is reduced to negligible values, they continue to undergo orbital decay at a location a with a rate (derived from Eqs. (12) & (13))

$$\dot{a} = \frac{\Delta E}{2\pi E} \left(\frac{GM}{a} \right)^{1/2}. \quad (24)$$

The characteristic orbital decay timescale,

$$\tau_a = \frac{a}{\dot{a}} = \frac{4\pi\rho_{\text{frag}}r_{\text{frag}}v_A\mu_0a^5}{3\alpha B_*^2 R_*^6}, \quad (25)$$

increases with both the fragment's size r_{frag} , density ρ_{frag} , and semi-major axis a .

During the fragments' orbit decay, the number of LPCs being replenished inside the tidal disruption radius can be estimated by,

$$N_{\text{LPC}} \simeq \dot{n}_{\text{LPC}}\tau_a. \quad (26)$$

In the limit $N_{\text{LPC}} \leq 1$, single disks would form from the debris of a LPC and decay before the arrival of another intruding LPC, such that N_{LPC} is equivalent to the duty cycle. In the limit $N_{\text{LPC}} > 1$, multiple inclined disks coexist, since the fragments of each LPC form a separate plane. This possibility may account for the coexistence of two or more rings around a 3 Gyr WD (Debes et al. 2019).

As the fragments undergo orbital decay and migrate inwards, the WD tidal force intensifies and the largest surviving fragments continue to be downsized $r_{\text{max,sur}} \propto q^{3/2}$ (see Fig. 2 and Eq. (5)). In a complementary study, Hogg et al. (2021) showed that under the influence of WDs' magnetic field, small fragments in the proximity of WDs may be cleared on timescale much shorter than that for the circularization of LPCs' orbits. It is not clear whether the distorted fields lines or overlapping Alfvén wings may interfere with each other in debris disks where the fragments contribute to a significant area filling factor. The efficiency of this magnetosphere-debris disk interaction remains an outstanding issue.

7. SUMMARY

We adopt a conventional scenario that the heavy-element enriched surfaces of many WDs is a manifestation of the continuous accretion of the relic building blocks from the planetary-assemblage era. Since the inferred delivery rates of metals onto these WDs is comparable to the cometary bombardment flux onto the Sun,

we use the Solar System as an analogue to ascribe the parent bodies of these pollutants to be LPCs originated from a population of residual planetesimals at locations comparable to the Oort cloud (located at $\sim 10^{3-4}$ au).

We address several key issues concerning this scenario:

1. the profusion of distant residual planetesimals,
2. the transformation of residual planetesimals into LPCs,
3. the tidal disruption of LPCs,
4. the formation of close-in disks from the circularized fragments, and
5. the accretion flow from dusty disks onto WDs.

For the origin of the residual planetesimals, we adopt the hypothesis that they form in the proximity of giant planets and are launched by the planetary perturbation to large distances from their host stars. We briefly recapitulate (Section 2) the subsequent pathways of their dynamical evolution as their host stars age. For discussions on the dominant physical effects, it is helpful to categorize the chronology into epochs of:

1. planet formation,
2. natal gaseous depletion and planetesimal scattering,
3. dispersal of cohort-star clusters,
4. secular evolution due to Galactic tides, passing GMCs and stars,
5. host stars' asymptotic-giant and mass-loss phase, and
6. WD cooling sequences.

The pivotal physical effects include:

1. planetary scattering due to close encounters, resonant and secular perturbation;
2. external perturbation due to Galactic tides, passing stars and GMCs;
3. dispersal of volatile components and orbital expansion during the host stars' post-main-sequence evolution;
4. planetesimals' material strength and internal composition; and
5. host WD luminosity, tidal and magnetic fields.

The main assumption of our scenario is that giant planets are common around WDs and their main-sequence progenitors. This assumption is tenable since such planets are common around stars more massive than the Sun, including WD progenitors. These planets' contribution is essential for the relocation of a rich population of residual planetesimals from their neighborhood to large distances from their host stars, analogous to the Oort cloud in the Solar System. At the outlying regions of host stars' gravitational domain, external perturbation can lead to a continuous injection of LPCs over Gyr timescales. Although such giant planets may also slow down and temporarily interrupt the gradual decrease of residual planetesimals' pericenter distances and their conversion into LPCs, this planetary barrier is dynamically permeable and LPCs can effectively bypass it as shown in the context of the Solar System.

We show (Section 3) that LPCs on nearly parabolic orbits can undergo tidal disruption provided their pericenter distances are within a fraction of the solar radius. However, these fragments generally follow the orbits of their LPC parent bodies. In order for them to be accreted onto the compact WDs, their semi-major axis must be greatly reduced through both angular momentum and energy loss. We show (Section 4) that around magnetized WDs, the fragments excite Alfvén waves during their closest approach and the resulting magnetic torque induces them to undergo orbital decay and circularization. Based on our analytic results and numerical confirmation (Section 5), we suggest this

magnetic interaction is a promising process for delivering heavy elements to the proximity of the WDs.

This magnetic interaction may further remove angular momentum and energy from the fragments after their orbits are circularized. In addition to magnetic breaking, the last leg of their journey to WD photospheres involves many additional physical processes including the Yarkovsky and YORP effects, PR drag, rotational and tidal downsizing, sublimation, collisional break-ups of fragments, viscous diffusion, and magnetosphere-disk interaction (Rafikov 2011; Veras et al. 2014, 2015b; Hogg et al. 2021). In an effort to model the IR excess around metal-enriched WDs, we plan to address these issues in a subsequent investigation.

ACKNOWLEDGMENTS

The authors thank an anonymous referee for careful reading of the manuscript and helpful suggestions. We also thank Roman Rafikov, Dimitri Veras, Xiaochen Zheng, and Simon Portegies Zwart for useful discussions and comments. S.-F.L. acknowledges support from National Natural Science Foundation of China under grant number 11903089 and from Guangdong Basic and Applied Basic Research Foundation under grant number 2021B1515020090 and 2019B030302001. Y.Z. acknowledges funding from the Université Côte d'Azur "Individual grants for young researchers" program of IDEX JEDI and the European Union's Horizon 2020 research and innovation program under grant agreement No. 870377 (project NEO-MAPP).

Software: REBOUND (Rein & Liu 2012), REBOUNDx (Tamayo et al. 2020)

REFERENCES

- Adams, F. C. 2010, *ARA&A*, 48, 47
- Adams, F. C., Anderson, K. R., & Bloch, A. M. 2013, *Monthly Notices of the Royal Astronomical Society*, 432, 438. <https://doi.org/10.1093/mnras/stt479>
- Andrews, S. M., Huang, J., Pérez, L. M., et al. 2018, *ApJL*, 869, L41
- Barber, S. D., Patterson, A. J., Kilic, M., et al. 2012, *The Astrophysical Journal*, 760, 26. <https://doi.org/10.1088/0004-637x/760/1/26>
- Bareither, C. A., Edil, T. B., Benson, C. H., & Mickelson, D. M. 2008, *Journal of geotechnical and geoenvironmental engineering*, 134, 1476
- Barrientos, M., & Chanamé, J. 2021, arXiv e-prints, arXiv:2102.07790
- Boe, B., Jedicke, R., Meech, K. J., et al. 2019, *Icarus*, 333, 252
- Bromley, B. C., & Kenyon, S. J. 2019, *The Astrophysical Journal*, 876, 17. <https://doi.org/10.3847/1538-4357/ab12e9>
- Brown, J. C., Veras, D., & Gnsicke, B. T. 2017, *Monthly Notices of the Royal Astronomical Society*, 468, 1575. <https://doi.org/10.1093/mnras/stx428>
- Carry, B. 2012, *Planetary and Space Science*, 73, 98, solar System science before and after Gaia. <http://www.sciencedirect.com/science/article/pii/S0032063312000773>
- Chen, D.-C., Zhou, J.-L., Xie, J.-W., et al. 2019, *Nature Astronomy*, 3, 69
- Cumming, A., Butler, R. P., Marcy, G. W., et al. 2008, *PASP*, 120, 531
- Debes, J. H., & Sigurdsson, S. 2002, *The Astrophysical Journal*, 572, 556. <https://doi.org/10.1086/340291>

- Debes, J. H., Thévenot, M., Kuchner, M. J., et al. 2019, *ApJL*, 872, L25
- Dones, L., Brasser, R., Kaib, N., & Rickman, H. 2015, *SSRv*, 197, 191
- Drell, S. D., Foley, H. M., & Ruderman, M. A. 1965, *Journal of Geophysical Research (1896-1977)*, 70, 3131
- Duncan, M., Quinn, T., & Tremaine, S. 1987, *AJ*, 94, 1330
- . 1988, *ApJL*, 328, L69
- Everhart, E. 1967, *The Astronomical Journal*, 72, 1002
- Fabrycky, D. C., Lissauer, J. J., Ragozzine, D., et al. 2014, *ApJ*, 790, 146
- Farihi, J. 2016, *New Astronomy Reviews*, 71, 9 .
<http://www.sciencedirect.com/science/article/pii/S1387647315300075>
- Farihi, J., Jura, M., & Zuckerman, B. 2009, *ApJ*, 694, 805
- Farihi, J., von Hippel, T., & Pringle, J. E. 2017, *Monthly Notices of the Royal Astronomical Society: Letters*, 471, L145. <https://doi.org/10.1093/mnrasl/slx122>
- Fernández, J. A. 1997, *Icarus*, 129, 106
- Fernández, J. A., & Ip, W. H. 1981, *Icarus*, 47, 470
- . 1984, *Icarus*, 58, 109
- Ferrario, L., de Martino, D., & Gänsicke, B. T. 2015, *Space Science Reviews*, 191, 111
- Ferrario, L., & Wickramasinghe, D. T. 2005, *MNRAS*, 356, 615
- Francis, P. J. 2005, *The Astrophysical Journal*, 635, 1348
- Fraser, W. C., Brown, M. E., Morbidelli, A., Parker, A., & Batygin, K. 2014, *ApJ*, 782, 100
- Gomes, R., Levison, H. F., Tsiganis, K., & Morbidelli, A. 2005, *Nature*, 435, 466
- Grishin, E., & Veras, D. 2019, *MNRAS*, 489, 168
- Hadjidemetriou, J. D. 1963, *Icarus*, 2, 440 . <http://www.sciencedirect.com/science/article/pii/0019103563900721>
- Hamers, A. S., & Portegies Zwart, S. F. 2016, *Monthly Notices of the Royal Astronomical Society: Letters*, 462, L84. <https://doi.org/10.1093/mnrasl/slwl134>
- Hanse, J., Jílková, L., Portegies Zwart, S. F., & Pelupessy, F. I. 2017, *Monthly Notices of the Royal Astronomical Society*, 473, 5432
- Hayashi, C., Nakazawa, K., & Nakagawa, Y. 1985, in *Protostars and Planets II*, ed. D. C. Black & M. S. Matthews, 1100–1153
- Heisler, J., & Tremaine, S. 1986, *Icarus*, 65, 13
- Hermes, J. J., Gänsicke, B. T., Kawaler, S. D., et al. 2017, *ApJS*, 232, 23
- Hestroffer, D., Sánchez, P., Staron, L., et al. 2019, *The Astronomy and Astrophysics Review*, 27, 6
- Hills, J. G. 1981, *AJ*, 86, 1730
- Hogg, M. A., Cutter, R., & Wynn, G. A. 2021, *MNRAS*, 500, 2986
- Hollands, M. A., Gnsicke, B. T., & Koester, D. 2015, *Monthly Notices of the Royal Astronomical Society*, 450, 681. <https://doi.org/10.1093/mnras/stv570>
- Holsapple, K. A. 2007, *Icarus*, 187, 500
- Holsapple, K. A., & Michel, P. 2008, *Icarus*, 193, 283
- Howard, A. W., Marcy, G. W., Bryson, S. T., et al. 2012, *ApJS*, 201, 15
- Hurley, J. R., Pols, O. R., & Tout, C. A. 2000, *MNRAS*, 315, 543
- Ida, S., & Lin, D. N. C. 2004, *ApJ*, 604, 388
- Ida, S., Lin, D. N. C., & Nagasawa, M. 2013, *ApJ*, 775, 42
- Isern, J., García-Berro, E., Külebi, B., & Lorén-Aguilar, P. 2017, *The Astrophysical Journal*, 836, L28. <https://doi.org/10.3847/2041-8213/aa5eae>
- Jura, M. 2003, *The Astrophysical Journal*, 584, L91. <https://doi.org/10.1086/374036>
- Kaib, N. A., & Quinn, T. 2009, *Science*, 325, 1234. <https://science.sciencemag.org/content/325/5945/1234>
- Kawka, A., Vennes, S., Ferrario, L., & Paunzen, E. 2019, *Monthly Notices of the Royal Astronomical Society*, 482, 5201. <https://doi.org/10.1093/mnras/sty3048>
- Kenyon, S. J., & Bromley, B. C. 2017, *The Astrophysical Journal*, 844, 116. <https://doi.org/10.3847/1538-4357/aa7b85>
- King, A. R. 1993, *Monthly Notices of the Royal Astronomical Society*, 261, 144. <https://doi.org/10.1093/mnras/261.1.144>
- Koester, D., Dreizler, S., Weidemann, V., & Allard, N. F. 1998, *A&A*, 338, 612
- Koester, D., Gänsicke, B. T., & Farihi, J. 2014, *A&A*, 566, A34. <https://doi.org/10.1051/0004-6361/201423691>
- Kratter, K. M., & Perets, H. B. 2012, *The Astrophysical Journal*, 753, 91. <https://doi.org/10.1088/0004-637x/753/1/91>
- Levison, H. F., Dones, L., & Duncan, M. J. 2001, *AJ*, 121, 2253
- Levison, H. F., Duncan, M. J., Dones, L., & Gladman, B. J. 2006, *Icarus*, 184, 619
- Long, F., Pinilla, P., Herczeg, G. J., et al. 2018, *ApJ*, 869, 17
- Malamud, U., Grishin, E., & Brouwers, M. 2021, *MNRAS*, 501, 3806
- Malamud, U., & Perets, H. B. 2020, *Monthly Notices of the Royal Astronomical Society*, 492, 5561. <https://doi.org/10.1093/mnras/staa142>
- Manser, C. J., Gnsicke, B. T., Gentile Fusillo, N. P., et al. 2020, *Monthly Notices of the Royal Astronomical Society*, 493, 2127. <https://doi.org/10.1093/mnras/staa359>

- Manser, C. J., Gänsicke, B. T., Ettl, S., et al. 2019, *Science*, 364, 66.
<https://science.sciencemag.org/content/364/6435/66>
- Meech, K. J., Hainaut, O. R., & Marsden, B. G. 2004, *Icarus*, 170, 463
- Morbidelli, A., Nesvorný, D., Bottke, W. F., & Marchi, S. 2021, *Icarus*, 356, 114256
- Mullally, F., Kilic, M., Reach, W. T., et al. 2007, *ApJS*, 171, 206
- Nagasawa, M., Lin, D. N. C., & Thommes, E. 2005, *ApJ*, 635, 578
- Neslušan, L. 2007, *Astronomy & Astrophysics*, 461, 741
- Neubauer, F. 1980, *Journal of Geophysical Research: Space Physics*, 85, 1171.
<https://doi.org/10.1029/JA085iA03p01171>
- O'Connor, C. E., & Lai, D. 2020, *MNRAS*, 498, 4005.
<https://ui.adsabs.harvard.edu/abs/2020MNRAS.498.4005O>
- Oort, J. H. 1950, *BAN*, 11, 91
- Petigura, E. A., Marcy, G. W., & Howard, A. W. 2013, *ApJ*, 770, 69
- Pohl, L., & Britt, D. T. 2020, *Meteoritics & Planetary Science*, 55, 962. <https://doi.org/10.1111/maps.13449>
- Portegies Zwart, S., Torres, S., Pelupessy, I., Bédorf, J., & Cai, M. X. 2018, *Monthly Notices of the Royal Astronomical Society: Letters*, 479, L17
- Punzo, D., Capuzzo-Dolcetta, R., & Portegies Zwart, S. 2014, *MNRAS*, 444, 2808
- Rafikov, R. R. 2011, *The Astrophysical Journal*, 732, L3.
<https://doi.org/10.1088/2041-8205/732/1/13>
- . 2018, *The Astrophysical Journal*, 861, 35
- Rafikov, R. R., & Garmilla, J. A. 2012, *The Astrophysical Journal*, 760, 123.
<https://doi.org/10.1088/0004-637x/760/2/123>
- Rein, H., & Liu, S. F. 2012, *A&A*, 537, A128
- Rein, H., & Spiegel, D. S. 2015, *MNRAS*, 446, 1424
- Richardson, D. C., Leinhardt, Z. M., Melosh, H. J., & Michel, P. 2002, in *Asteroids III*, ed. W. F. Bottke, A. Cellino, P. Paolicchi, & P. R. Binzel (Tucson: Univ. of Arizona), 501–515
- Scheeres, D., Hartzell, C., Sánchez, P., & Swift, M. 2010, *Icarus*, 210, 968
- Schröder, K.-P., & Connors, R. 2008, *Monthly Notices of the Royal Astronomical Society*, 386, 155.
<https://doi.org/10.1111/j.1365-2966.2008.13022.x>
- Spurzem, R., Giersz, M., Heggge, D. C., & Lin, D. N. C. 2009, *ApJ*, 697, 458
- Sridhar, S., & Tremaine, S. 1992, *Icarus*, 95, 86 .
<http://www.sciencedirect.com/science/article/pii/S001910359290193B>
- Tamayo, D., Rein, H., Shi, P., & Hernandez, D. M. 2020, *MNRAS*, 491, 2885
- Tremblay, P.-E., Cummings, J., Kalirai, J. S., et al. 2016, *Monthly Notices of the Royal Astronomical Society*, 461, 2100. <https://doi.org/10.1093/mnras/stw1447>
- Tsiganis, K., Gomes, R., Morbidelli, A., & Levison, H. F. 2005, *Nature*, 435, 459
- Vanderbosch, Z., Hermes, J. J., Dennihy, E., et al. 2020, *The Astrophysical Journal*, 897, 171.
<https://doi.org/10.3847/1538-4357/ab9649>
- Vanderburg, A., Johnson, J. A., Rappaport, S., et al. 2015, *Nature*, 526, 546
- Veras, D. 2016, *Royal Society Open Science*, 3, 150571
- Veras, D., Ettl, S., & Gänsicke, B. T. 2015a, *Monthly Notices of the Royal Astronomical Society*, 452, 1945.
<https://doi.org/10.1093/mnras/stv1417>
- Veras, D., & Heng, K. 2020, *Monthly Notices of the Royal Astronomical Society*, 496, 2292.
<https://doi.org/10.1093/mnras/staa1632>
- Veras, D., Higuchi, A., & Ida, S. 2019, *Monthly Notices of the Royal Astronomical Society*, 485, 708.
<https://doi.org/10.1093/mnras/stz421>
- Veras, D., Leinhardt, Z. M., Bonsor, A., & Gänsicke, B. T. 2014, *Monthly Notices of the Royal Astronomical Society*, 445, 2244. <https://doi.org/10.1093/mnras/stu1871>
- Veras, D., Leinhardt, Z. M., Ettl, S., & Gänsicke, B. T. 2015b, *Monthly Notices of the Royal Astronomical Society*, 451, 3453.
<https://doi.org/10.1093/mnras/stv1195>
- Veras, D., & Wolszczan, A. 2019, *Monthly Notices of the Royal Astronomical Society*, 488, 153.
<https://doi.org/10.1093/mnras/stz1721>
- Veras, D., Wyatt, M. C., Mustill, A. J., Bonsor, A., & Eldridge, J. J. 2011, *MNRAS*, 417, 2104
- Veras, D., Reichert, K., Flammini Dotti, F., et al. 2020, *MNRAS*, 493, 5062
- von Hippel, T., Kuchner, M. J., Kilic, M., Mullally, F., & Reach, W. T. 2007, *The Astrophysical Journal*, 662, 544.
<https://doi.org/10.1086/518108>
- Walsh, K. J., Jawin, E. R., Ballouz, R.-L., et al. 2019, *Nature Geoscience*, 12, 242
- Weissman, P. R. 1983, *A&A*, 118, 90
- Weissman, P. R., & Levison, H. F. 1997, *The Astrophysical Journal*, 488, L133
- Wiegert, P., & Tremaine, S. 1999, *Icarus*, 137, 84
- Xu, S., Rappaport, S., van Lieshout, R., et al. 2017, *Monthly Notices of the Royal Astronomical Society*, 474, 4795. <https://doi.org/10.1093/mnras/stx3023>
- Zhang, Y., & Lin, D. N. C. 2020, *Nature astronomy*, 4, 852

- Zhang, Y., & Michel, P. 2020, *Astronomy & Astrophysics*, 640, A102
- Zhang, Y., Richardson, D. C., Barnouin, O. S., et al. 2018, *The Astrophysical Journal*, 857, 15
- . 2017, *Icarus*, 294, 98
- Zheng, X., Lin, D. N. C., & Kouwenhoven, M. B. N. 2017a, *ApJ*, 836, 207
- Zheng, X., Lin, D. N. C., Kouwenhoven, M. B. N., Mao, S., & Zhang, X. 2017b, *ApJ*, 849, 98
- Zhou, J.-L., & Lin, D. N. C. 2007, *The Astrophysical Journal*, 666, 447
- Zuckerman, B., & Becklin, E. 1987, *Nature*, 330, 138
- Zuckerman, B., Koester, D., Reid, I. N., & Hunsch, M. 2003, *The Astrophysical Journal*, 596, 477.
<https://doi.org/10.1086/377492>